Bioactive Materials 39 (2024) 59–73

Contents lists available at ScienceDirect

Bioactive Materials

journal homepage: www.keaipublishing.com/en/journals/bioactive-materials

Dynamic microphysiological system chip platform for high-throughput, customizable, and multi-dimensional drug screening

Yuxuan Zhu [a,e,1], Deming Jiang [a,c,1], Yong Qiu [a], Xin Liu [a], Yuhan Bian [a], Shichao Tian [a], Xiandi Wang [a], K. Jimmy Hsia [b], Hao Wan [a,c,***], Liujing Zhuang [a,e,**], Ping Wang [a,c,d,e,*]

[a] Biosensor National Special Laboratory, Key Laboratory of Biomedical Engineering of Ministry of Education, Department of Biomedical Engineering, Zhejiang University, Hangzhou, Zhejiang, 310027, China
[b] Schools of Mechanical & Aerospace Engineering, of Chemical & Biomedical Engineering, Nanyang Technological University, 639798, Singapore
[c] Cancer Center, Binjiang Institute of Zhejiang University, Hangzhou, 310027, China
[d] The MOE Frontier Science Center for Brain Science & Brain-machine Integration, Zhejiang University, Hangzhou, 310027, China
[e] State Key Laboratory of Transducer Technology, Chinese Academy of Sciences, Shanghai, 200050, China

ARTICLE INFO

Keywords:
Microphysiological system
Organ-on-a-chip
Biomimetics
High throughput
Multidimensional drug screening

ABSTRACT

Spheroids and organoids have attracted significant attention as innovative models for disease modeling and drug screening. By employing diverse types of spheroids or organoids, it is feasible to establish microphysiological systems that enhance the precision of disease modeling and offer more dependable and comprehensive drug screening. High-throughput microphysiological systems that support optional, parallel testing of multiple drugs have promising applications in personalized medical treatment and drug research. However, establishing such a system is highly challenging and requires a multidisciplinary approach. This study introduces a dynamic Microphysiological System Chip Platform (MSCP) with multiple functional microstructures that encompass the mentioned advantages. We developed a high-throughput lung cancer spheroids model and an intestine-liver-heart-lung cancer microphysiological system for conducting parallel testing on four anti-lung cancer drugs, demonstrating the feasibility of the MSCP. This microphysiological system combines microscale and macroscale biomimetics to enable a comprehensive assessment of drug efficacy and side effects. Moreover, the microphysiological system enables evaluation of the real pharmacological effect of drug molecules reaching the target lesion after absorption by normal organs through fluid-based physiological communication. The MSCP could serves as a valuable platform for microphysiological system research, making significant contributions to disease modeling, drug development, and personalized medical treatment.

1. Introduction

Anti-cancer drug discovery involves multiple stages, from drug development to clinical approval. However, many drugs fail in clinical trials due to efficacy and safety issues [1]. The limitations of current preclinical models hinder the accurate representation of human diseases [2]. Improving assessment methods and enhancing *in vitro* models are crucial for more reliable preclinical research results. *In vitro* 2D cell and *in vivo* animal models are commonly used for assessing drug safety and efficacy [3]. While *in vivo* model construction is time-consuming, *in vitro* 2D cell models lack the *in vivo* microenvironment for accurate evaluations. Moreover, testing drug efficacy and side effects separately in these models can lead to variations between experiments, causing discrepancies between preclinical and clinical stages. Therefore, developing

Peer review under responsibility of KeAi Communications Co., Ltd.
* Corresponding author. Biosensor National Special Laboratory, Key Laboratory of Biomedical Engineering of Ministry of Education, Department of Biomedical Engineering, Zhejiang University, Hangzhou, Zhejiang, 310027, China.
** Corresponding author. Biosensor National Special Laboratory, Key Laboratory of Biomedical Engineering of Ministry of Education, Department of Biomedical Engineering, Zhejiang University, Hangzhou, Zhejiang, 310027, China.
*** Corresponding author. Biosensor National Special Laboratory, Key Laboratory of Biomedical Engineering of Ministry of Education, Department of Biomedical Engineering, Zhejiang University, Hangzhou, Zhejiang, 310027, China.
E-mail addresses: wh1816@zju.edu.cn (H. Wan), zhuangliujing@zju.edu.cn (L. Zhuang), cnpwang@zju.edu.cn (P. Wang).
[1] These authors contributed equally to this work.

https://doi.org/10.1016/j.bioactmat.2024.05.019
Received 18 January 2024; Received in revised form 13 April 2024; Accepted 8 May 2024
Available online 17 May 2024

more efficient and comprehensive preclinical screening models is essential for successful anti-cancer drug development.

In anti-cancer drug development, *in vitro* 3D cell models such as spheroids and organoids are gaining wide attention. Spheroids mimic complex *in vivo* microenvironments and offer better gene expression through 3D cell-cell contact [4–6]. Organoids, with organ-like structures, exhibit strong drug resistance [7,8]. These advantages make spheroids and organoids ideal models for preclinical drug development. Different types of organoids have been reported, such as the brain [9–11], heart [12–14], liver [15–17], pancreas [18,19], lung cancer [20–22], etc. These organoids have been extensively applied to research organ development [23], disease modeling [24], and drug screening [25]. However, the lengthy and manual culture process of spheroids and organoids introduces individual differences and high costs. Additionally, these 3D model in static cultures lack fluidic connections for constructing microphysiological systems. Therefore, an automated, high throughput, and fluidic interconnection platform may lead to breakthroughs in spheroids and organoid applications.

Microfluidic chips, as customizable and automated devices, are widely used in spheroid and organoid culture and applications. They enable the creation of various organ-on-chip models, such as retina-on-chip [26], brain-on-chip [27–29], heart-on-chip [30,31], and liver-on-chip [32,33]. Furthermore, microfluidic platforms with structures like microwell [34] and micropillar [35] arrays facilitate high-throughput spheroids and organoids culture. Besides, multi-organ microphysiological systems are established to mimic inter-organ communication and systemic diseases [36–38]. These systems combine macroscale and microscale biomimetics, offering insights into

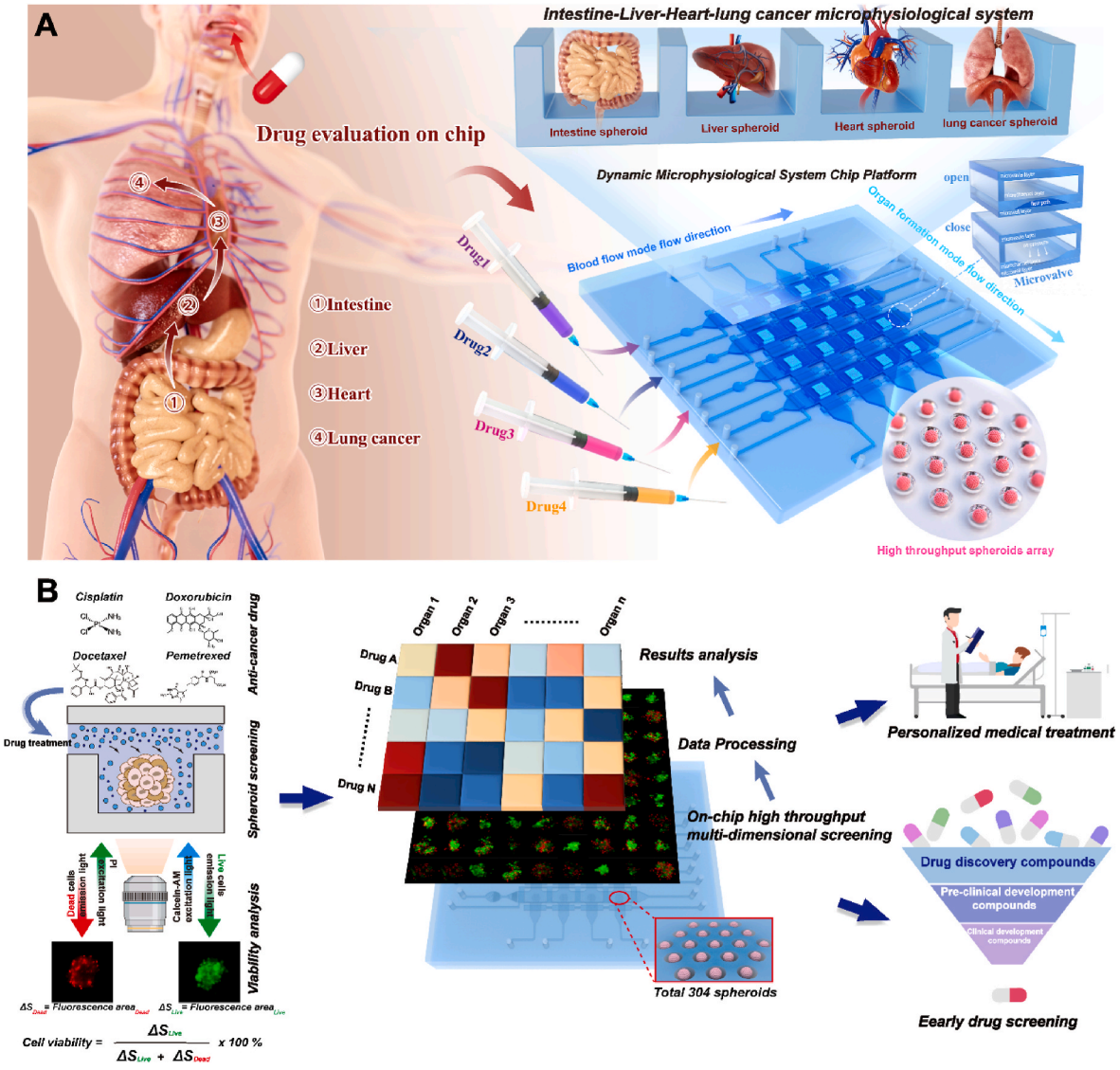

Fig. 1. The Microphysiological System Chip Platform (MSCP) enables the construction of microphysiological systems as well as comprehensive drug screening. (**A**), Left: schematic diagram of oral anti-lung cancer drug absorption process, which shows that drug is absorbed in the intestine and then through blood vessels flow through each vital organ, such as liver, heart, and lung. Right: The MSCP can construct a high-throughput intestine-liver-heart-lung cancer microphysiological system to simultaneously evaluate four different drugs. This on-chip microphysiological system mimics the *in vivo* processes depicted in the left diagram to realize comprehensive drug evaluation with high throughput and concurrent testing of multiple drugs. (**B**), Schematic diagram of the basic detection principle, the platform application process, and prospect. Anti-cancer drugs act on the spheroid in the microwell, and the spheroids' cell viability is reflected by microscopic detection of live/dead staining fluorescence. The MSCP integrates 4 × 4 microwell arrays that can simultaneously cultivate 304 spheroids. After spheroids' cell viability data processing and analysis, comprehensive drug screening results will be exhibited by hot map. The utilization of high-throughput microphysiological systems, coupled with the simultaneous evaluation of multiple drugs, has rendered the MSCP an expedient and effective platform for personalized medicine and drug development.

interorgan crosstalk, metabolism, and immunity [39–41]. By incorporating cancer spheroids and organoids, these systems can assess pharmacokinetics, pharmacodynamics, and overall pharmacological responses [42]. This systematic evaluation is crucial for drug discovery, development, and personalized medicine [43–45]. Through microfluidic technology, the organ-on-a-chip can construct specific microphysiological systems corresponding to the design of the chip structure [46–48]. However, constructing microphysiological systems with less structural specificity, high throughput, and customizable using microfluidic technology is highly challenging.

To address these challenges, we have developed a customizable and high-throughput microphysiological system chip platform (MSCP) for comprehensive drug screening. As shown in Fig. 1, the MSCP integrates a microvalves array to dynamically switch between two biomimetic flow path modes: organ formation mode and blood flow mode. This on-chip dynamic switching allows for the combination of up to four spheroids, either of the same or different types, to create a high-throughput drug testing model or microphysiological system. To evaluate the feasibility of the MSCP, we cultured A549 lung cancer spheroids in a high-throughput manner to simultaneously assess the efficacy of four chemotherapy drugs: cisplatin, docetaxel, pemetrexed, and doxorubicin. Furthermore, we established a microphysiological system that combines the small intestine (FHs 74 Int), liver (THLE-2), heart (HL-1), and lung cancer (A549) spheroids to multi-dimensional assess the potential side effects of the aforementioned oral anti-lung cancer drugs and the decrease in drug efficacy resulting from absorption by these normal

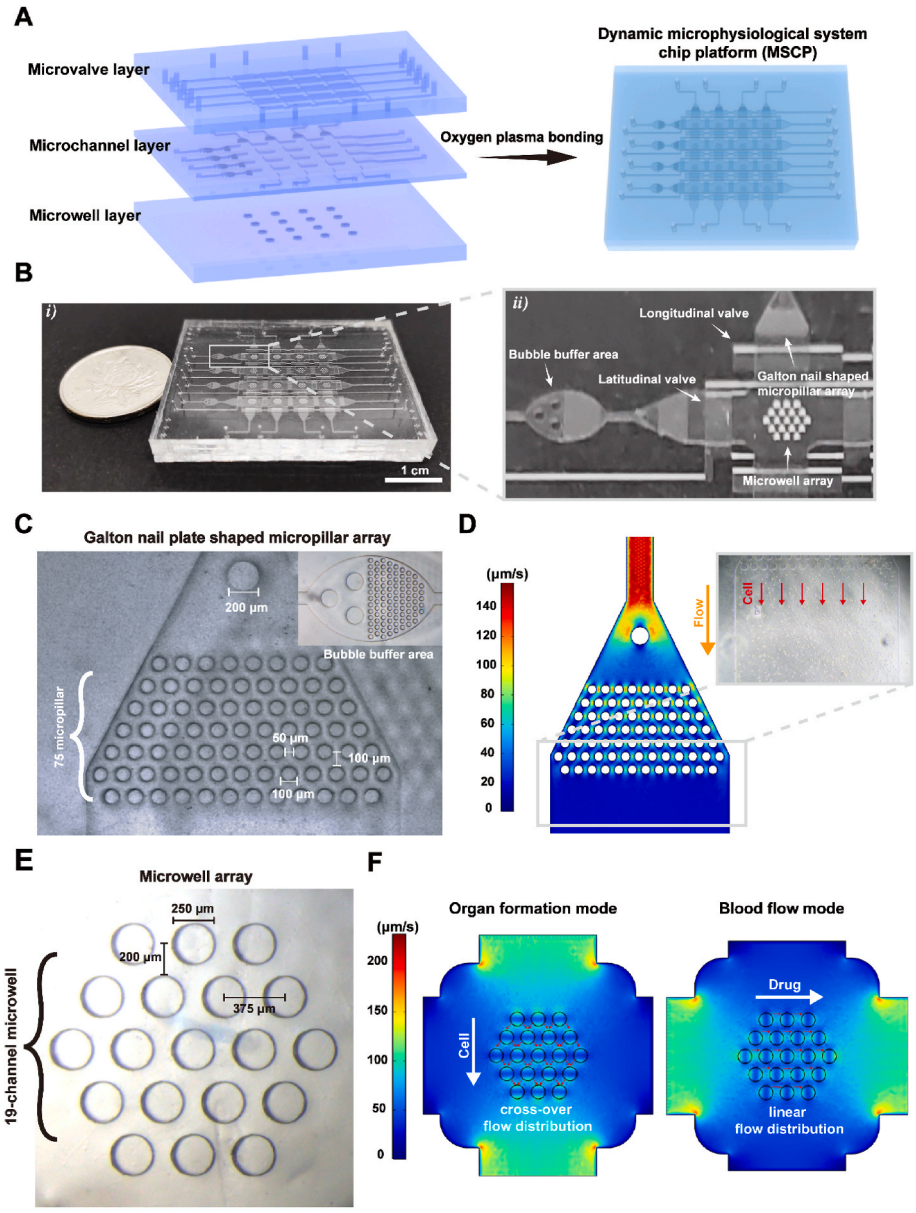

Fig. 2. Design of the MSCP. (**A**), An exploded schematic illustration of the MSCP. The MSCP is fabricated by irreversible bonding of the microvalve layer, microchannel layer, and microwell layer. (**B**), Photograph and microscopic image of the MSCP. ***i)*** Photograph of the MSCP to exhibit the size of the MSCP (scale bar = 1 cm). ***ii)*** An enlarged view of part of the MSCP shows the main functional structures in the MSCP. The MSCP consists of five main functional structures: bubble buffer areas, latitudinal and longitudinal valve arrays, Galton nail plate shaped micropillar arrays, and microwell arrays. (**C**), The microscopic image shows the details of the Galton nail plate shaped micropillar array and bubble buffer area. (**D**), Numerically simulated flow velocity distribution of the Galton nail plate shaped micropillar array (initial flow velocity is 100 μm/s, corresponding to a flow rate of 9×10^{-3} μL/min) illustrates that it significantly improves the uniformity of cell distribution. (**E**), Microscopic image shows the design details of a microwell array. (**F**), Numerically simulated flow velocity distribution of the hexagonal arrangement of the microwell array (initial flow velocity is 100 μm/s, corresponding to a flow rate of 0.63 μL/min).

organs. The results of these investigations demonstrate that the MSCP, with its ability to rapidly construct high-throughput microphysiological systems and enable simultaneous evaluation of multiple drugs, serves as a robust platform for researching microphysiological systems. It holds promising applications in personalized medical treatment, drug development, and disease modeling.

2. Results

2.1. Dynamic microphysiological system chip platform design

The MSCP combines the microvalve and microwell array to realize the construction of high-throughput and customizable microphysiological systems. For multiple functional microstructures integrated into the MSCP, Three PDMS layers—microvalve layer, microchannel layer, and microwell layer are designed. Oxygen plasma is applied to irreversible bond these layers (Fig. 2A). In Fig. 2B–a photograph and enlarged view demonstrate the overall appearance and microstructure details of the MSCP. As Fig. 2B *i)* shows, The dimensions of the MSCP are slightly larger than a coin, with specific measurements of 5 cm in length, 4 cm in width, and a thickness of 0.6 cm. Fig. 2B *ii)* is the enlarged view of part of the MSCP and shows its main functional microstructures. The MSCP consists of five main functional microstructures: bubble buffer areas, latitudinal and longitudinal valve arrays, Galton nail plate shaped micropillar arrays, and microwell arrays. These microstructures are distributed in different PDMS layers. The microvalve layer mainly consists of latitudinal and longitudinal valve arrays. The microchannel layer, situated at the central tier of the MSCP, is engineered to be thinly fabricated to optimize the closure efficiency of the microvalve. This layer mainly has four longitudinal cell injection channels, four latitudinal drug injection channels, and corresponding inlets and outlets. Besides, the MSCP has a total of 16 spheroid culture chambers, which are set at each intersection of the longitudinal channel and latitudinal channel. These spheroid culture chambers are aligned to the square regions of the microvalve layer, thus making microvalves separate. The MSCP has 16 microwell arrays, which are located corresponding to the upper microchannel layer's spheroid culture chamber. The bubble is a common problem that tremendously impacts microfluidic devices. There are two types of bubble interference generation reasons: dead zone of microstructure and bubbles introduced by liquid injection. We found that vacuuming the PDMS-based device, which is immersed in ethanol, can make it fill with ethanol without bubbles, and then ethanol can be replaced by another buffer for further use. This operation markedly reduces the bubble interference caused by the microstructure dead zone. In the microchannel layer, the bubbles buffer area (Fig. 2C upper right corner) is set at each latitudinal drug injection channel inlet to avoid bubbles or impurities introduced by liquid injection. Impurities and bubbles will be trapped by the micropillar array in the buffer area. Because of the air permeability property of PDMS, the positive pressure generated by fluid injection will make the bubbles trapped in the micropillar array disappear. As Fig. 2C shows, a Galton nail plate shaped micropillar array is designed for uniform-size spheroid formation. The uniform distribution of cells in cell suspension is a crucial factor in spheroid size uniformity. Poor spheroid size uniformity may cause differences in drug resistance between spheroids that lead to inaccuracy drug resistance results. The Galton nail plate shape micropillar array is set at each longitudinal cell injection inlet. As Fig. 2D shows, numerically simulated results of flow velocities in the Galton nail plate shaped micropillar array are exhibited to explain its function (initial flow velocity is 100 μm/s, corresponding to a flow rate of 9×10^{-3} μL/min). For bifurcation tree structure (Fig. S1), less bifurcation means less cell redistribution, so cells in suspension may unevenly distribute, which makes it accumulate at the dead zone of the microchannel. The Galton nail plate shape micropillar array significantly increases the cell redistribution times and reduces structural dead zones, leading cells to be more evenly distributed in suspension (movie.S1). The microwell array (Fig. 2E) in the MSCP integrates 19-channel microwells that have been arranged in a hexagonal configuration for uniform cell deposition (movie.S2). Totally 304 microwells can be used for the 3D culture. The microwell size is a crucial parameter related to spheroids formation size and cell viability. The size of a microwell is 250 × 250 μm (diameter × deep) for cultivating spheroids whose diameter not exceeding 250 μm. Furthermore, in Fig. 2F, through flow velocity simulation of the hexagonal arrangement of the microwell array, we demonstrate that in the organ formation mode of MSCP, the cross-sectional flow distribution assists the cells in the cell suspension to traverse each microwell, resulting in a uniform deposition into the microwell array. Additionally, when MSCP is in the blood flow mode, the linear flow distribution in MSCP helps reduce the generation of concentration differences to simulate the flow of effective drug molecules in the human bloodstream. Fig. S2 demonstrates the spheroids array formation process through the microwell array. Uniform-size spheroids array can be established by following this procedure: (1) inject cell suspension into the MSCP with a fast flow rate (50–100 μL/min) to lead cells completely cover the microwell array, (2) allow the MSCP to rest on a flat surface for an appropriate amount of time for cells to deposit into the microwell array, (3) gently wash the redundant cells that have deposited outside of the microwell array, and (4) continue to inject culture medium to maintain an indispensable cultivation environment until cells aggregate and form spheroids. By arranging the microwell array into a hexagonal shape, injecting cells suspension at a faster flow rate, and then depositing cells, a uniform-sized spheroid array can be generated.

2.2. Microvalve optimization and biomimetic flow path construction

The MSCP utilizes the "push down" microvalves array to control the flow direction and is compatible with microwell. There are two types of microvalves in the MSCP: latitudinal microvalves and longitudinal microvalves. The whole microvalves array comprises 20 latitudinal microvalves and 20 longitudinal microvalves. Fig. 3A shows the schematic diagram and photograph of the "push down" microvalve in the open and closed state. In the photograph, an empty opened and closed microvalve is displayed to show the difference between the microchannel before and after the microvalve is activated. Air pressure is applied to activate the microvalve, leading to the microchannel layer deformation to seal the flow path (movie.S3–S4). Because of the air permeability of PDMS, before applying this kind of pneumatic microvalve to liquid-related applications, the channels in the microvalve layer must be full of liquid to prevent gas from permeating to the bottom channels. In this situation, the microvalve layer deformation is caused by hydraulic, which air pressure introduces. The microvalve array is driven by external air pressure, and the air pressure magnitude has a direct effect on the degree of microvalve array sealing. It is essential to find an optimal valve control pressure to prevent leakage and avoid reduction of service life of the MSCP caused by too high air pressure. We have observed the degree of the longitudinal valve (Fig. 3B) and the latitudinal valve (Fig. 3C) deformation after applying 100 mbar–700 mbar air pressure. The higher the air pressure applied, the tighter the longitudinal and latitudinal valves closed. Low closing air pressure (<100 mbar) can not completely seal the microvalve, affecting the channels' independence. High closing air pressure (>700 mbar) may cause the MSCP delamination and reduce the device's service life. Finally, 500 mbar air pressure is selected for closing the microvalves. With this optimized air pressure, the microvalves can keep closing without leakage for prolonged use while the flow velocity is 100 μL/min.

To construct an *in vitro* microphysiological system, the parallel culture chamber must be separated at the spheroids formation stage to prevent undesirable cell interaction between different spheroids. Besides, a fluidic connection needs to be built between different spheroids for physiology communication after spheroids formation. The MSCP has two biomimetic flow path modes—organ formation mode and blood flow mode-to simultaneously realize culturing of different types of

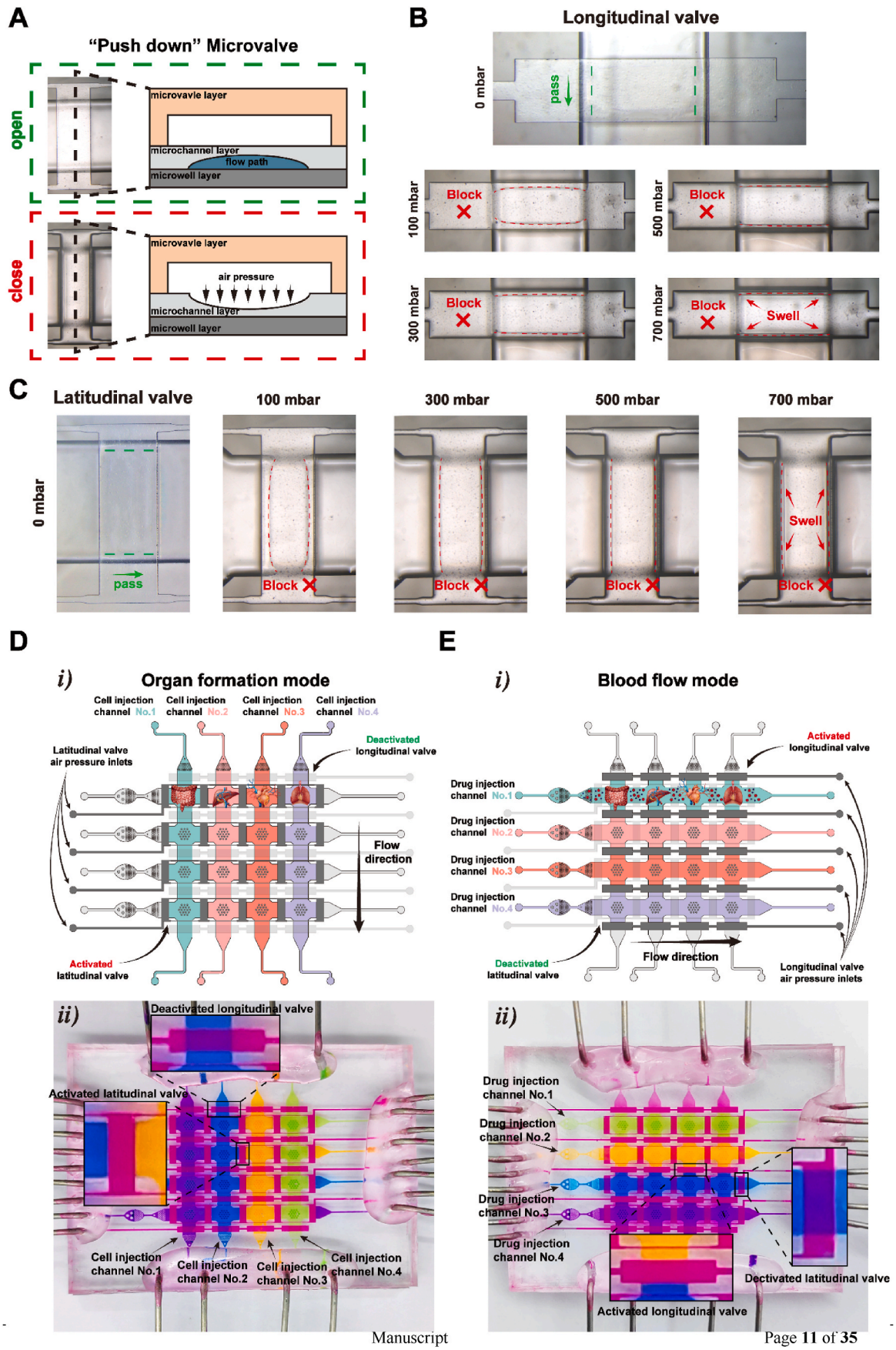

(caption on next page)

Fig. 3. Microvalve optimization and two biomimetic flow path mode construction of the MSCP. (**A**), Cross-section schematic diagram of activated and deactivated "push down" microvalve. (**B–C**), Activating air pressure optimization for the longitudinal valve (**B**) and the latitudinal valve (**C**). The air pressure being tested went from 100 to 700 mbar. (**D**), Schematic diagram and photograph of the organ formation mode. ***i)*** The schematic diagram of the organ formation mode. Different spheroids arrays can be independently cultivated in each cell injection channel in this mode. The latitudinal microvalve array blocks all the drug injection channels. All the longitudinal microvalves are open to ensure that four cell injection channels are unobstructed. The flow direction of the MSCP is longitudinal. No.1-No.4 Cell injection channels are filled into four colors (green, pink, red, and purple) to illustrate the independence between each cell injection channel. Activated latitudinal microvalves are filled into gray. ***ii)*** The photograph of the organ formation mode. Corresponding to the schematic diagram, all the cell injection channels are dyed into different colors to illustrate the channel's independence. (**E**), Schematic diagram and photograph of the blood flow mode. ***i)*** The schematic diagram of the blood flow mode. In this mode, fluidic cross-talk is established to mimic *in vivo* blood vessels' physiology communication function. The longitudinal microvalve array blocks all the cell injection channels. All the latitudinal microvalves are open to ensure that four drug injection channels are unobstructed. The flow direction of the MSCP is latitudinal. No.1-No.4 Drug injection channels are filled into four colors (green, pink, red, and purple) to illustrate the independence between each drug injection channel. Activated longitudinal microvalves are filled into gray. ***ii)*** The photograph of the blood flow mode. Corresponding to the schematic diagram, all the drug injection channels are dyed into different colors to illustrate the channel's independence.

spheroids on-chip and construction of physiology communication between spheroids array, thus establishing microphysiological systems. As the schematic diagram shown in Fig. 3D *i)*, in the organ formation mode, four group latitudinal microvalves are activated by applying air pressure from inlets, and longitudinal microvalves are kept deactivated. In this situation, the flow direction in the MSCP is longitudinal, and latitudinal microvalves separate four cell injection channels. As shown in the photograph in Fig. 3D *ii)*, each cell injection channel was dyed into different colors to demonstrate each channel's independence. Through the organ formation mode, each cell injection channel can inject a conspecific cell to form a high-throughput spheroids drug evaluation model or inject heterospecific cells to establish microphysiological systems (Fig. S3). After spheroids formation, the MSCP can switch to the blood flow mode by reversing the activated and deactivated state of the longitudinal microvalve and latitudinal microvalve. As the schematic diagram shown in Fig. 3E *i)*, in the blood flow mode, all cell injection channels are sealed by the longitudinal microvalve, and the flow direction changes from longitudinal to latitudinal. Longitudinal microvalves separate four parallel drug injection channels. As shown in the photograph in Fig. 3E *ii)*, four parallel drug injection channels were dyed into different colors to demonstrate that drugs can be injected into each drug injection channel without mutual interference. The independence between each cell injection channel at organ formation mode is important, and after each cell injection channel is dyed into different colors with no color crosstalk, a video is recorded of the color mutual interference when deactivated latitudinal microvalves to prove the effectiveness of the latitudinal microvalves (movie.S5). Utilizing the same video method to prove blood flow mode channels' independence (movie.S6). In the organ formation mode, four independent parallel cell injection channels can generate distinct spheroid arrays without intermingling of cells and liquid. In the blood flow mode, the MSCP enables fluidic communication between different spheroid arrays, simulating the physiological communication function of *in vivo* blood vessels. Additionally, four parallel drug injection channels allow the MSCP to simultaneously assess four different concentrations of a drug, or four different drugs, thereby enhancing drug screening efficiency. In conclusion, the dynamic switching between these two biomimetic flow modes enables the MSCP to flexibly construct customizable microphysiological systems, while also enabling simultaneous evaluation of multiple drugs in different dimensions (drug efficacy and side effects). These advantages serve as the foundation for further research on microphysiological systems, drug development, and the potential applications of personalized medicine.

2.3. Characterization of intestinal, liver, heart, and lung cancer spheroids

We have generated the high throughput intestine (FHs 74 Int), liver (THLE-2), heart (HL-1), and lung cancer (A549) spheroids array and tested their viability and histological morphology variation. Additionally, we have conducted functional characterization of four different spheroids. Fig. 4A shows the HE staining and immunofluorescent staining functional characterization of intestinal, liver, heart, and lung cancer spheroids. The HE staining results of four different spheroids showed their distinctive morphological characteristics. For cultured FHs 74 Int spheroids, CDX2/Villin were used as dual markers for functional identification. CDX2, an intestine-specific transcription factor expressed in the nuclei of intestinal epithelial cells, and Villin, a specific marker for intestinal absorptive cells, were utilized [49,50]. The identification results showed that FHs 74 Int intestine spheroids expressed CDX2/Villin, indicating their exhibit the basic characteristics of intestinal epithelium and functionality as intestinal absorptive cells. Likewise, dual marker functional identification of ALBumin/CYP2C9 was performed for THLE-2 spheroids. ALBumin, specifically synthesized by liver cells in the human body, and CYP2C9, an important drug-metabolizing enzyme in the human liver, were used [51,52]. The results demonstrated that THLE-2 liver spheroids expressed ALBumin/CYP2C9, indicating their basic protein expression resembling liver cells and capability for drug metabolism. Furthermore, dual marker identification of α-Actin/cTnT was conducted for HL-1 spheroids. α-Actin, usually expressed in various muscles, such as skeletal muscle, cardiac muscle, and smooth muscle, and cTnT, specifically expressed in cardiac muscle cells, were employed [53,54]. The results showed that HL-1 heart spheroids expressed α-Actin/cTnT, indicating their basic characteristics of cardiac muscle. Lastly, dual marker functional identification of E-cadherin/CK7 was performed for A549 spheroids. E-cadherin, a key component of adherens junctions and indispensable for cell adhesion and maintenance of cell epithelial phenotype, and CK7, specifically expressed in lung cancer tissue, were utilized [55,56]. Immunofluorescent results demonstrated that A549 lung cancer spheroids expressed E-cadherin/CK7, indicating their characteristics resembling lung cancer tissue. Fig. 4B shows the four kinds of spheroids array after 72 h culturing. In the organ formation mode, almost the same number of cells were dispersed into each microwell. After 72 h culturing, a uniform-size spheroids array was formed, which is crucial to improve the accuracy of the drug evaluation. Fig. S4 displays the histological morphology variation of four kinds of spheroids during 120 h. The findings demonstrate that the size of intestinal spheroids (FHs 74 Int) continuously increased over a period of five days. Additionally, their compactness also exhibited a rising trend during the culturing process, as evidenced by the dim opacity observed within the spheroid. Liver spheroids (THLE-2) rapidly aggregated after deposition and displayed a steady increase in size within five days. These spheroids exhibited a spherical shape. However, after 72 h of culturing, cell detritus progressively appeared. Heart spheroids (HL-1) have the smallest size after five days of culturing. They swiftly formed within 24 h of cell deposition, and their margin became smooth by 48 h. However, at 72 h, the aggregated cells within HL-1 spheroids began to detach, resulting in a slight decrease in size. Lung cancer spheroids (A549) remained granular within 24 h of cell deposition, with the contour of the spheroid margin only becoming smooth after 48 h of culturing. After 120 h, A549 spheroids became denser, and their size significantly increased. The diameter statistics of four types of spheroids within five days are shown in Fig. 4C. The results show that the size of the THLE-2 spheroid kept increasing, and it had a maximum average size after five days of culturing. The minimum spheroid average size after five days of

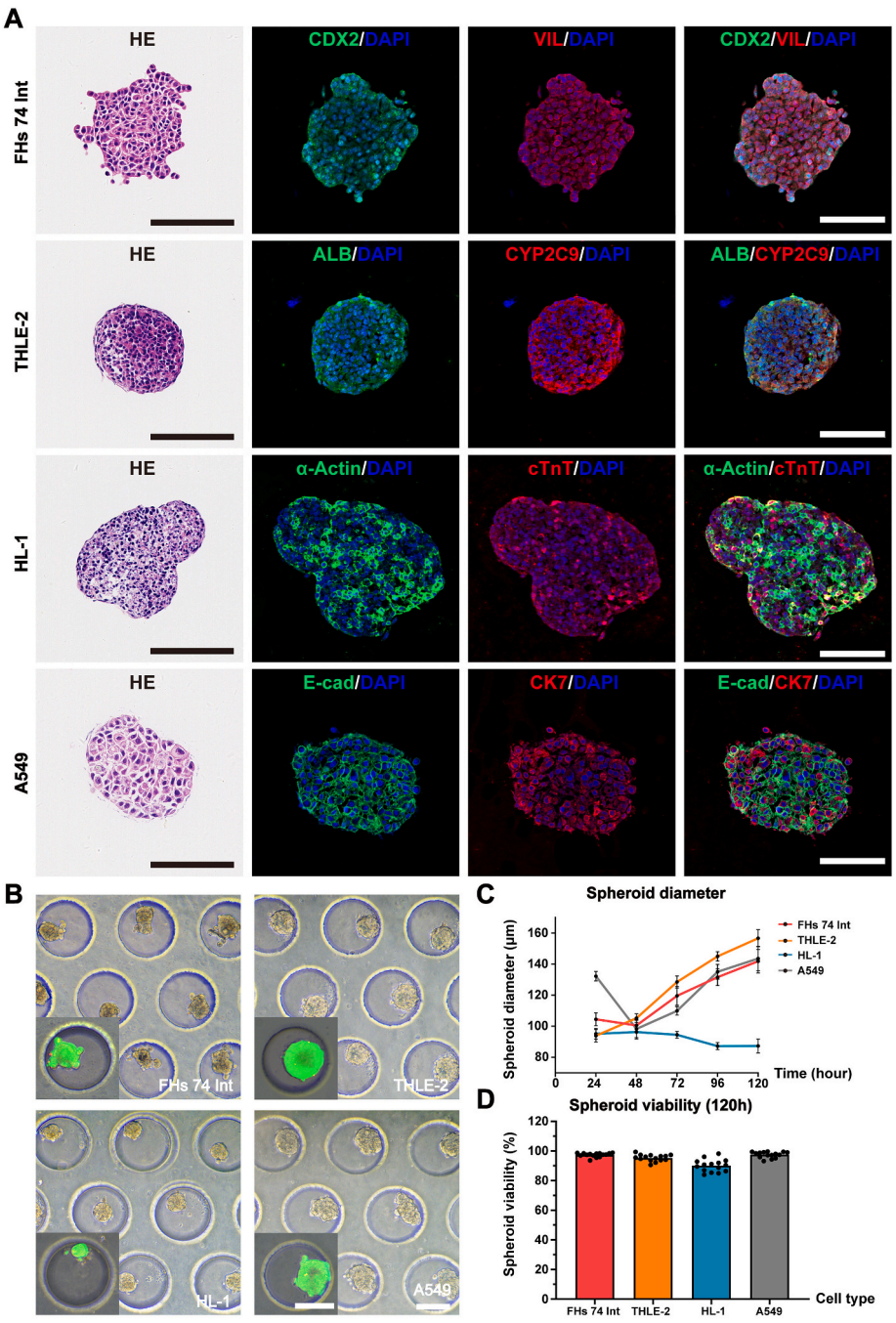

Fig. 4. Characterization of the function, viability, and size of different types of spheroids. (**A**), HE and immunofluorescent images characterizing the morphological characteristics and the specific functions of four different types of spheroids. (**B**), A549, FHs 74 Int, HL-1, and THLE-2 spheroids array after formation (scale bar = 150 μm). (**C**), Spheroids diameter statistics within five days (n = 6 biological replicates). (**D**), Viability of the four kinds of spheroids after 120 h of culturing (n = 15 biological replicates).

culturing is the HL-1 spheroid, and its size decreased after 72 h of culturing. The A549 spheroids had a maximum average size at 24 h and then significantly decreased at 48 h. The FHs 74 Int spheroids also had this phenomenon. The average diameter of the FHs 74 Int, THLE-2, HL-1, and A549 spheroids at 48 h is 100.02 μm, 107.13 μm, 99.29 μm, and 99.83 μm. The range of average diameter after 48 h culturing is small enough (<10 μm) to be adopted as a cultivation time intersection point for these four kinds of spheroids. With this conclusion, the oral anti-lung cancer drug evaluation microphysiological system with these four kinds of spheroids can quickly be constructed within 48 h with a relatively homogeneous diameter. Except for size, the viability of spheroids is also an indispensable factor that possibly influences the evaluation accuracy. Fig. 4D shows the viability of four types of spheroids after five days of cultivation. The results show that FHs 74 Int, THLE-2, HL-1, and A549 spheroids kept high average cell viability (>90 %), which is enough to form a high viability oral anti-lung cancer drug evaluation microphysiological system within five days to ensure the accuracy of drug evaluation.

2.4. High throughput anti-lung cancer drugs evaluation

The MSCP has 304 microwells to high-throughput cultivate spheroids and four parallel drug injection channels to simultaneously evaluate four different anti-lung cancer drugs within an exam cycle. Fig. 5A shows the drug evaluation process scheme of the MSCP. For high throughput lung cancer spheroids formatting, the MSCP was switched to the organ formation mode, and A549 cell suspension was injected into the MSCP through all parallel cell injection channels at day 0. Kept cell medium injected into the MSCP through cell injection channels to maintain the cell growth environment. After two days of culturing, A549 cells aggregated and formed spheroids in the microwell array. Switched the MSCP into blood flow mode, then injected four first-line anti-lung cancer drugs through all parallel drug injection channels. After 24 h drug treatment, a live/dead fluorescence assay was applied to evaluate drug efficacy.

With this evaluation process, we tested the efficacy of first-line anti-lung cancer drug cisplatin, docetaxel, pemetrexed, and doxorubicin by high throughput culturing A549 spheroids with the MSCP. A549 is a non-small cell lung cancer epithelial cell line which widely used for anti-lung cancer drug development [57] and the study of disease modeling [58]. The 3D structure of the spheroids makes its drug resistance commonly stronger than 2D cultivation with the same kind of cell. We tested each anti-lung cancer drug in five dosing concentrations of 10 μM, 33 μM, 100 μM, 333 μM, and 1000 μM which are higher than general 2D drug evaluation concentration. Drug effects positively correlate to treatment time, and prolonged drug affecting time probably causes drug efficacy evaluation results to be higher than the actual situation because low-concentration drugs could also kill many cells when treatment time is prolonged. As Fig. 5B shows, A549 spheroids kept high viability at four kinds of drug treatment at 10 μM in 24 h, and almost all cells died at 1000 μM treatment in 24 h. This result showed that the IC_{50} values of the four drugs were between 10 μM and 1000 μM after 24 h of treatment, which proved the feasibility of drug concentration interval and treatment time. Fig. 5C shows the IC_{50} curves of four drugs affecting A549 spheroids obtained through live/dead staining imaging in the MSCP, and the IC_{50} curves of the four drugs on A549 spheroids cultured in U-shaped plates analyzed quantitatively using the 3D Cell Viability Assay. The results of live/dead staining in the MSCP shows, A549 spheroids had the most potent drug response to doxorubicin with an IC_{50} of 25.2 μM. Cisplatin had the second drug efficacy to A549 spheroids with an IC_{50} of 109.5 μM. The drug efficacy of docetaxel was slightly weaker than cisplatin, and it had an IC_{50} of 159.7 μM. A549 spheroids had the weakest drug response to pemetrexed with an IC_{50} of 440.1 μM. The 3D Cell Viability Assay quantitative analysis results showed that the IC_{50} value of cisplatin was 114.8 μM, docetaxel was 214.7 μM, pemetrexed was 652 μM, and doxorubicin was 31.04 μM. Compared to the results of high-throughput drug testing with the MSCP, the drug efficacy

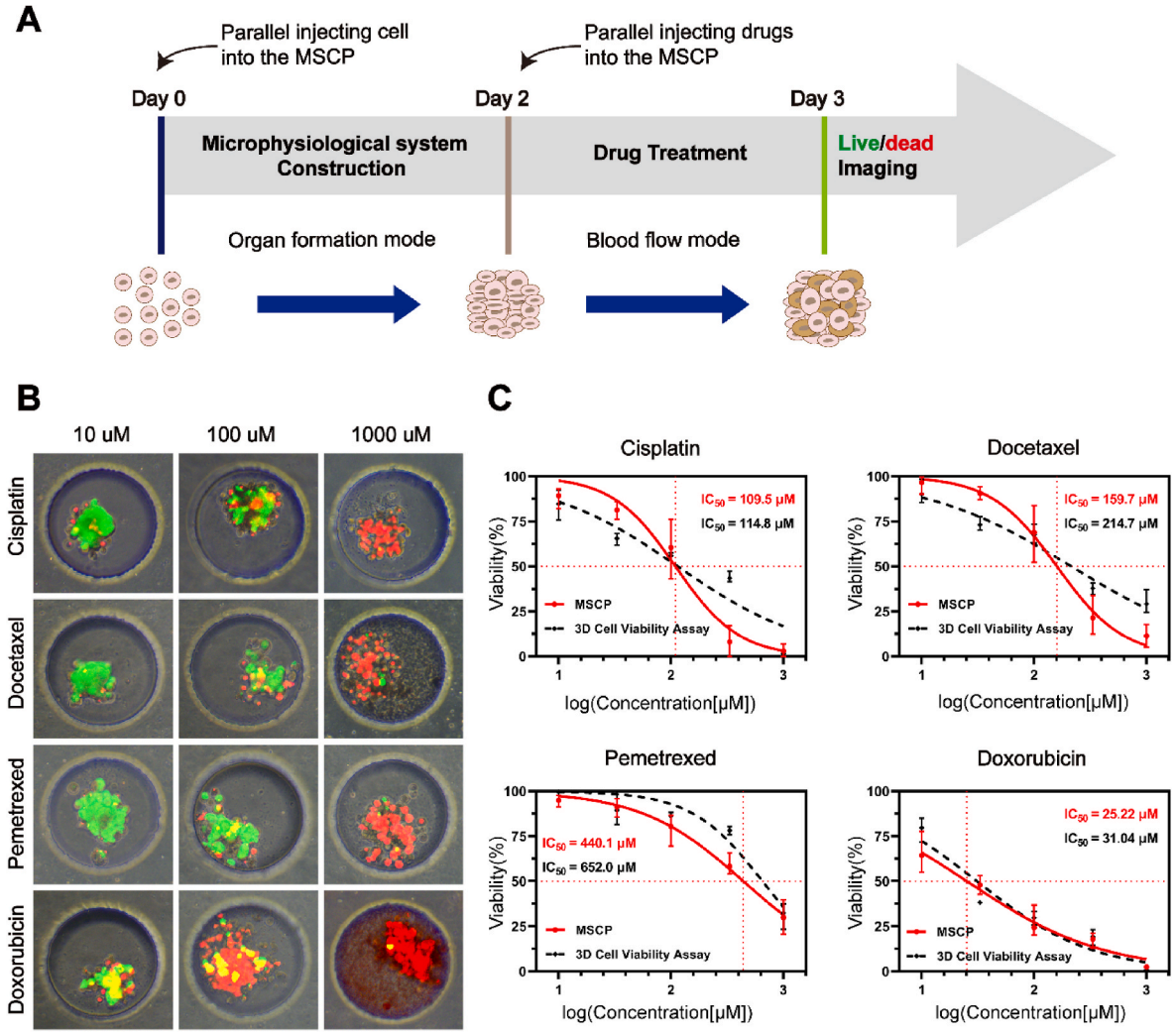

Fig. 5. High-throughput evaluates different first-line anti-lung cancer drug efficacy. (**A**), Drug evaluation process scheme of the MSCP. (**B**), Bright-field and live/dead staining picture stack results of lung cancer spheroid A549 affected by cisplatin, docetaxel, pemetrexed, and doxorubicin at 10 μM, 100 μM, and 1000 μM after 24 h treatment. (**C**), The IC_{50} curve results of four drugs on A549 spheroids with the MSCP and 3D cell viability assay.

distribution of the four drugs was consistent, with doxorubicin still having the strongest efficacy, followed by cisplatin, docetaxel, and pemetrexed. Furthermore, the IC_{50} values of the 3D Cell Viability Assay for the four drugs on A549 spheroids are higher compared to the IC_{50} values from the live/dead staining fluorescence test in the MSCP. This may be due to the drug concentration in the culture medium of A549 spheroids decreasing with cell metabolism during drug testing without flow condition, whereas the drug concentration remains constant in flow-perfused conditions, thus more accurately reflecting the actual drug efficacy. In conclusion, doxorubicin has the strongest drug efficacy, and pemetrexed has the weakest drug efficacy among these four kinds of drugs. This experiment proves that the MSCP can be a convenient platform for rapid and high throughput obtaining accurate drug evaluation results.

2.5. Intestine-liver-heart-lung cancer microphysiological system construction and multi-dimensional drug evaluation

Oral anti-lung cancer drugs are absorbed in the small intestine, flow through the blood vessels to various essential organs, and reach the target cancer area. In the oral drug delivery process in the human body, organs may absorb drug molecules, leading to unexpected decreases in drug efficacy and inevitable drug side effects. Drug screening research usually focuses on the independent evaluation of drug efficacy or side effects rather than the comprehensive evaluation of these two aspects. Besides, *in vivo* physiology communication between each organ is difficult to remodel *in vitro*. It is, therefore, significant to develop a microphysiological system that can efficiently gather extensive side effects data for multiple drugs on various organs, as well as efficacy data on lesions.

Through the two biomimetic flow path modes of the MSCP, we constructed an oral anti-lung cancer drug evaluation microphysiological system with intestine (FHs 74 Int), liver (THLE-2), heart (HL-1), and lung cancer (A549) spheroid. With this microphysiological system, we simultaneously evaluated the drug efficacy of cisplatin, pemetrexed, doxorubicin, and docetaxel after the normal organ absorption and the side effects of these drugs on the intestine, liver, and heart. As Fig. 6A shows, when the MSCP switches to the blood flow mode, corresponding to the *in vivo* oral anti-lung cancer drug flow process, drug molecules in the MSCP flow through the intestine, liver, and heart spheroids and then reach the lung cancer spheroids. IC_{50} concentrations (obtained from previous experiments) of directly treated A549 lung cancer spheroids, that cisplatin (109.5 μM), pemetrexed (440.1 μM), doxorubicin (25.2 μM), and docetaxel (159.7 μM) are used to treat intestine-liver-heart-lung cancer microphysiological system. Therefore, comparatively analyze when the direct drug treatment efficacy of lung cancer spheroids is the same, the side effects of the four drugs on the intestines, liver, and heart, as well as the reduced efficacy caused by the absorption of these drugs by the normal organs. Fig. 6B shows the effects of four drugs on each type of tested spheroid. The results show that compared to the control group, four tested drugs significantly decreased the cell viability of four spheroids. The results of four kinds of drug effects on intestine spheroids highlight that doxorubicin significantly inhibited the viability of intestine spheroids, causing its mean viability to descend to 68.6 %. Besides, the other three drugs caused intestine spheroids' mean viability to descend to 95.2 %, 86.6 %, and 87.1 % (data order is correlated to the drug arrangement order in the image, from left to right). In addition, docetaxel significantly inhibited liver spheroids growth, causing its mean viability to descend to 26 %, and the other three drugs led the liver spheroids' mean viability to descend to 50.2 %, 46.1 %, and 52.3 %. Besides, doxorubicin significantly inhibited the growth of heart spheroids, causing the mean viability to descend to 32.6 %, and the other three drugs led the heart spheroids' mean viability to descend to 68.7 %, 57.3 %, and 53 %. For lung cancer spheroids, we used the IC_{50} concentration of each anti-lung cancer drug tested in the previous experiment to treat the intestine-liver-heart-lung cancer microphysiological system, so the mean viability of it should be about 50 %. However, the mean viability of lung cancer spheroids after four anti-lung cancer drug treatments is 64.8 %, 64.3 %, 75.1 %, and 59.7 %, significantly higher than 50 %. This drug efficacy descent was caused by drug absorption by the previous normal spheroids in the flow path. Notably, this absorption effect was conspicuous for pemetrexed, causing lung cancer to keep a higher mean viability than the other three drugs. Fig. 6C shows the dark-field drug evaluation results of the intestine-liver-heart-lung cancer microphysiological system. In this image, the live cells of spheroids appear green, and the dead cells of spheroids appear red. The ratio of green pixels to the total fluorescence pixels reflects the spheroid's viability. Four anti-lung cancer drugs flowed through the intestine, liver, heart, and lung cancer spheroids to mimic *in vivo* physiology communication between organs. Fig. 6D displays the variation of spheroids viability along the flow path after the four drug treatments. The results indicate that each type of spheroid has varying degrees of viability descending after drug treatment. Although intestine spheroids are placed at the first position in the microphysiological system, it accurately reflects the drug response of intestine spheroids rather than an excessive decrease in cell viability compared to other types of spheroids. Besides, it can be seen from the statistical results that intestine spheroids and lung cancer spheroids keep relatively higher viability, and liver spheroids and heart spheroids are more vulnerable to drug influence. As Fig. 6E shows, the statistics results of mean viability are transformed into a drug toxicity hot map after standardization. As highlighted in this image, all four tested drugs have potential hepatotoxicity, and docetaxel has the strongest effect on the liver. In addition, pemetrexed, doxorubicin, and docetaxel have potential cardiac toxicity. Among these tested drugs, doxorubicin has the most potent effect on the heart. The findings of this experiment affirm that the MSCP is capable of effectively constructing customizable and high throughput microphysiological systems, such as the intestine-liver-heart-lung cancer model. Moreover, the MSCP features four parallel drug injection channels that enable simultaneous evaluation of various drugs with pre-constructing microphysiological systems, allowing for multidimensional drug assessment. Additionally, the 3D Cell Viability Assay was used to quantitatively test the drug efficacy on four different types of spheroid that cultured in U-shaped plates at the IC_{50} concentrations of the four drugs. Fig. 6F shows the radar pattern comparison to illustrate the differences between the quantitative test results and the MSCP test results. After cisplatin treatment, the viability results for spheroids in MSCP versus 3D Cell Viability Assay independent testing were as follows: A549 (65 % vs. 55 %), FHs 74 Int (95 % vs. 70 %), THLE-2 (50 % vs. 21 %), and HL1 (69 % vs. 42 %). Following pemetrexed treatment, the viability results for spheroids in MSCP versus independent testing were: A549 (75 % vs. 71 %), FHs 74 Int (87 % vs. 73 %), THLE-2 (46 % vs. 26 %), and HL1 (53 % vs. 42 %). With Doxorubicin treatment, the viability results for spheroids in MSCP versus independent testing were: A549 (60 % vs. 61 %), FHs 74 Int (69 % vs. 80 %), THLE-2 (52 % vs. 44 %), and HL1 (33 % vs. 14 %). Post Docetaxel treatment, the viability results for spheroids in MSCP versus independent testing were: A549 (64 % vs. 55 %), FHs 74 Int (87 % vs. 80 %), THLE-2 (26 % vs. 31 %), and HL1 (57 % vs. 72 %). These results showed that the pattern diagrams of the intestinal-liver-heart-lung cancer microphysiological system model constructed by MSCP were mostly consistent with the drug testing pattern diagram of the quantitative testing results of the four drugs on the four different spheroids. This further demonstrated the ability of the microphysiological system constructed by MSCP to simultaneously evaluate drug efficacy and side effects. Furthermore, for lung cancer A549 spheroids, cisplatin, pemetrexed and docetaxel tested in MSCP showed a decrease, possibly due to the decrease in drug concentration caused by the upstream absorption of intestinal, liver, and heart spheroids. This further indicates that using the microphysiological system constructed by MSCP for drug evaluation may simulate the real drug efficacy when drugs reach the lesion after metabolism in multiple human organs.

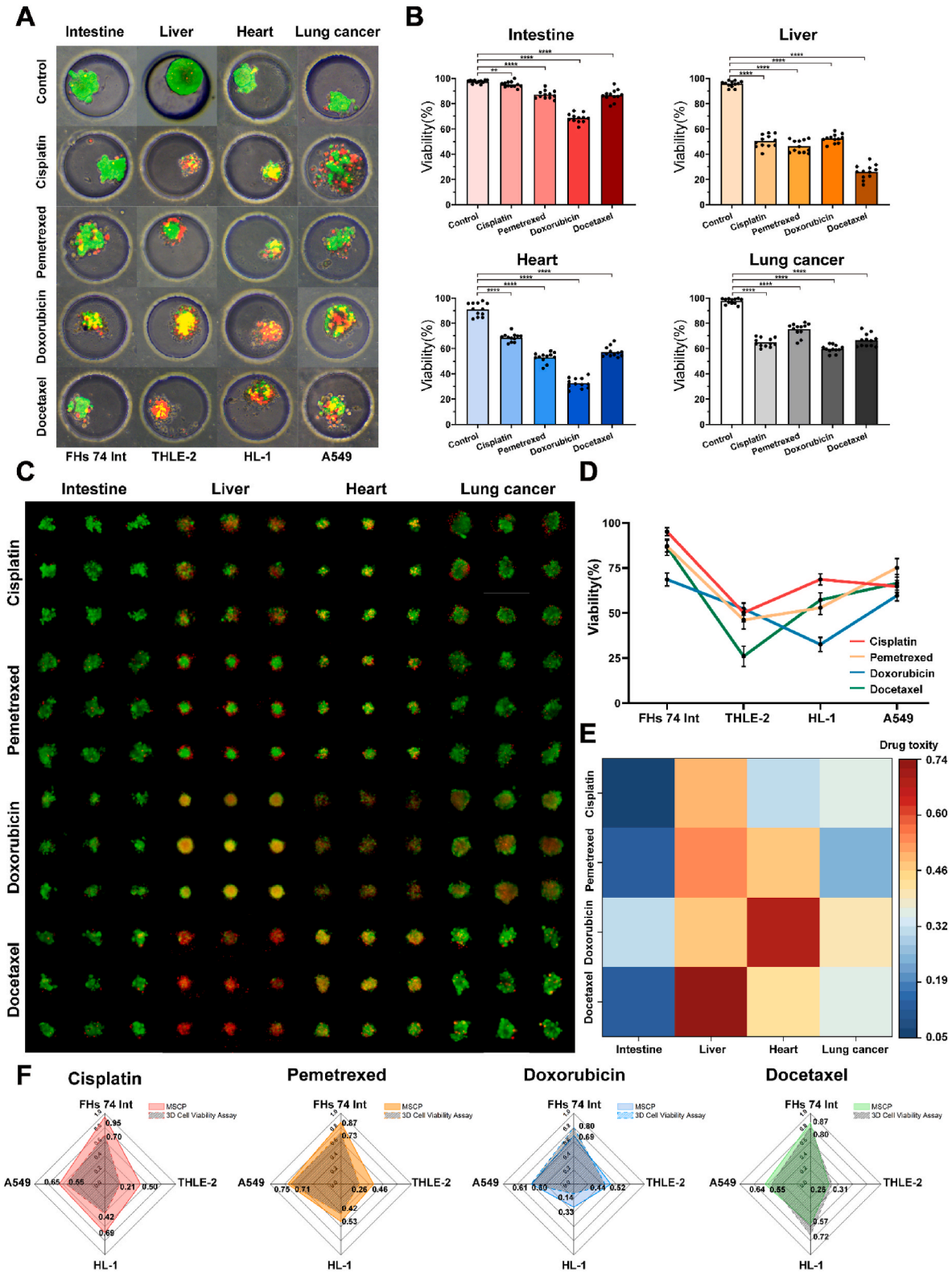

Fig. 6. Intestine-liver-heart-lung cancer microphysiological system for multidimensional drug evaluation. (**A**), Bright-field and live/dead staining picture stack results of intestine-liver-heart-lung cancer microphysiological system (red = dead cells, green = live cells). This microphysiological system model was treated with cisplatin, docetaxel, pemetrexed, and doxorubicin at IC_{50} concentration (Cisplatin, 109.5 μM; Pemetrexed, 440.1 μM; Doxorubicin, 25.2 μM; Docetaxel, 159.7 μM) which get by prior drug evaluation exam. (**B**), Mean viability statistics of each spheroid affected by four anti-lung cancer drugs (**$p < 0.01$, ****$p < 0.0001$, n = 12 biological replicates). (**C**), Dark-field drug evaluation results of the microphysiological system model. The results of nine biological replications for each organ to each drug are presented (3 × 3). The drug flows through the intestine, liver, and heart spheroids, reaching lung cancer spheroids. (**D**), Spheroids viability results along the drug flow direction (n = 12 biological replicates). (**E**), Drug toxicity hot map analysis results of the multidimensional drug evaluation. (**F**), Drug efficacy pattern radar comparison diagram between MSCP and 3D Cell Viability Assay.

3. Discussion

The MSCP integrates multiple layers of PDMS with different structures and functions to construct a platform with various functional microstructures. The MSCP incorporates an arrayed pneumatic microvalve system that enables dynamic switching between two biomimetic flow path modes. Based on these two biomimetic dynamic modes, a high-throughput drug efficacy evaluation model containing lung cancer spheroids (A549) and a microphysiological system model containing intestine (FHs 74 Int), liver (THLE-2), heart (HL-1), and lung cancer (A549) were constructed. Using the above models simultaneously evaluated the independent drug efficacy of four first-line oral anti-lung cancer drugs, their side effects on multiple organs in a multi-organ system, and the actual drug efficacy after absorption by organs. We believe that the MSCP, as a convenient, high-throughput, and customizable platform, has broad applications in early drug screening, customized construction of multiple drug evaluation models, and personalized medicine.

Due to the automation and high-throughput advantages of microfluidic technology, previous studies have reported the use of microfluidic platforms with microwell arrays to culture HT-29 spheroids uniformly and test anticancer drugs [59]. However, due to the low throughput (25 channels), it may have limitations in high-throughput applications such as early drug evaluation. The MSCP includes a total of 304 microwell channels, enabling the simultaneous on-chip culture of 304 spheroids of the same type for testing four different drugs. This greatly enhances the throughput of drug evaluation, allowing simultaneous assessment of four different drugs or different concentration gradients of the same drug, significantly shortening the experimental period and reducing repetitive operations. Additionally, studies have reported the use of high-throughput microwell arrays combined with live/dead staining fluorescence for culturing tumor organoids and conducting individual and combination tests of multiple drugs, implementing various drug combinations over time [60]. This platform integrates 200 microwell arrays and manually introduces spheroids or organoids cultured externally into each microwell for drug testing. Despite its high microwell throughput, this platform still has certain limitations in specific operations; for example, manually loading multiple microwells with spheroids or organoids is a very cumbersome process and may introduce more operational errors. Furthermore, non-in situ cultured organoids may experience unforeseen changes after being loaded onto the platform due to alterations in the culture environment. Due to the arrayed pneumatic microvalve system and microstructures that promote uniform spheroid size (hexagonal microwell array and Galton-nail shaped micropillar array), the MSCP can employ an automated culture scheme for introducing cell suspensions and allowing cells to settle and form spheroids in situ, reducing laborious manual operations and operational errors. Inspired by this article, the MSCP can also conduct combination tests of multiple drugs to expand its applications. A microfluidic platform combining microwells with an arrayed pump-valve system has also been reported for culturing high-throughput ovarian cancer (OC) spheroids and drug testing [61]. This platform uses a layout of 1 × 8 cultivation chambers and adopts gravity-driven automatic perfusion for sample introduction. While gravity-driven automatic perfusion eliminates the need for external pumping systems, the flow speed in the chip is uncontrollable, potentially resulting in inaccuracies in drug concentration gradients. Moreover, the 1 × 8 layout of cultivation chambers cannot simultaneously achieve the construction of a multi-organ integrated microphysiological system and enable testing of multiple different drugs with microphysiological system. The MSCP adopts a 4 × 4 layout of cultivation chambers and utilizes injection pumps to control flow speeds within the chip, enabling the construction of microphysiological systems based on four different spheroids and testing four different drugs simultaneously. Furthermore, studies have reported the construction of multi-organ integrated microphysiological systems using Multi-organ tissue chip [38]. However, due to the need for independent device structure designs for different organs on organ chips, there may be limitations in application scenarios. The MSCP uniformly adopts the microwell structure to cultivate different types of spheroids in each channel without the need for specific device designs, making it more versatile in various application scenarios. In summary, the MSCP combines the advantages of easy operation, high throughput, and customizability, allowing simultaneous testing of multiple drugs, demonstrating significant potential and expandability in practical applications.

The MSCP fabrication involves creating multi-layer molds with photolithography and casting PDMS layers using mature methods. Alignment and bonding of the three PDMS layers present challenges due to the irreversible feature of oxygen plasma bonding. Optimization can be achieved through glue bonding and fixtures to improve repeatability. Successful alignment leads to stable functionality and robust reproducibility of the MSCP.

The microphysiological system is a kind of biomimetic body-on-a-chip system [62]. It is the combination of micro and macro biomimetics. On the micro scale, each kind of spheroids and organoids model precisely mimics different organs' functions. On the macro scale, the microphysiological system constructs organ-to-organ crosstalk to mimic the physiological communication between each vital organ *in vivo*. This interesting combination allows for multidimensional biomimetic simulations using a single spheroid, organoid, or organ-on-a-chip, realizing the modeling of intricate diseases, and has broad application prospects in early drug screening and personalized medical treatment. A study introduced a PDMS-free multi-organoid microfluidic platform capable of accommodating up to 6 different organoids to construct a comprehensive microphysiological system [63]. Liver, cardiac, lung, testis, colon, and brain organoids cultured in 96-well format non-adherent round bottom plates can be implanted into this microfluidic platform for free combination to build a 6-tissue microphysiological system. With this system, they successfully verified liver organoids enable the metabolism of capecitabine and cyclophosphamide into activated toxic forms, resulting in downstream drug toxicities in other organoids. This result further proves the advantages of the microphysiological system in drug screening. However, this platform cannot in situ culture different spheroids or organoids and dynamically construct multiple microphysiological system. Oral anti-lung cancer drugs navigate through internal organs after ingestion, potentially causing side effects and decreasing effectiveness if absorbed by normal cells. Single spheroid models lack the ability to assess drugs comprehensively or simulate their passage through multiple organs. To evaluate oral anti-lung cancer drugs thoroughly, a microphysiological system mimicking drug flow through vital organs is essential for post-absorption efficacy assessment. Through the MSCP, we constructed an intestinal-liver-heart-lung cancer microphysiological system based on different spheroids and tested four first-line lung cancer drugs. The test results indicated that this microphysiological system could accurately assess the side effects of the four drugs on the intestine, liver, and heart simultaneously, as well as the actual efficacy of the drugs on lung cancer lesions after absorption by the above organs. The test results for drug side effects were consistent with previous studies [64–66], and ultimately, all four drugs showed varying degrees of decreased efficacy on lung cancer spheroids. This decrease in efficacy may more closely resemble the actual effects of the four oral drugs after ingestion, as the upstream intestine and liver spheroids may exhibit certain barrier and metabolic effects, respectively.

When utilizing MSCP to culture different types of spheroids, we discovered that the size and density of different types of spheroids varied due to the different growth rates between cells. We think that this difference is primarily due to the inherent size differences of different cell types. For example, the single-cell size of the intestinal cell line FHs 74 Int (~>15 μm) is larger than that of the liver cell line THLE-2 (~<10 μm). Due to the differences in single-cell size, culturing spheroids of the same size results in varying numbers of single cells in different types of

spheroids, leading to differences in nutrient requirements and overall metabolic rates of the spheroids. Using the same perfusion rate of culture medium can cause size differences between different types of spheroids. Moreover, there are differences in cell properties among different cells, such as single-cell metabolic rates and cell adhesion ability. For example, we observed that lung cancer spheroid A549 maintains a certain granular state even after 24 h of culture, showing inadequate aggregation, while liver spheroid THLE-2 typically appears as a smoothly spherical shape with good aggregation after 24 h of culture. Therefore, the size of A549 spheroids tends to initially decrease (aggregation) and then increase (growth), while the size of THLE-2 spheroids shows a continuous increase trend. Although there are differences in spheroid size, we believe that unlike organoids, spheroids exhibit stable functional characteristics from the beginning of forming a smooth spherical appearance, unlike organoids that need to mature from an immature phenotype gradually during self-assembly. However, although spheroids of different sizes possess functionality, the size differences still result in variations in functional levels. Larger spheroids, when exposed to drugs, exhibit stronger drug resistance compared to smaller spheroids due to their enhanced metabolic capacity and lower drug concentration reaching the inner cells. Therefore, maintaining consistent sizes among spheroids is essential to ensure the accuracy of the model. Culturing spheroids of uniform size is challenging due to the differences between various cell types. For the same type of spheroids, we use a microwell array approach for high-throughput construction of uniform-sized spheroid arrays. For different types of spheroids, given the numerous variables, our method involves identifying a time window with the minimal size difference among spheroids of different cell types at the same cell density. The results indicate that when the cell density in the cell suspension is the same, the size difference among the four different spheroids is smallest ($<$10 μm) after 48 h of spheroid culture, making it a suitable time window for drug administration, as at this point, the four different spheroids exhibit uniform size and consistent functional levels.

However, MSCP also has certain limitations. For example, it can only simulate up to four different organs' spheroids, limiting the construction of a more diverse microphysiological system. Besides, in the constructed intestinal-liver-heart-lung cancer microphysiological system, there are still some organs missing that may affect the actual effects of drugs, such as the kidneys, fat, and the vascular barrier. Additionally, we constructed a microphysiological system with unidirectional flow using MSCP. By creating a microphysiological system with circulating flow, a better simulation of the drug's impact on the entire system can be achieved to evaluate long-term drug metabolism. In future work, further expansion of the arrayed structure of MSCP can be carried out to integrate more types of spheroids to realize the construction of a microphysiological system with more than four different organs. Furthermore, based on the existing characteristics of MSCP, using primary cells to construct more realistic spheroids and creating induced organoids from induced pluripotent stem cells on-chip are also an important direction to enhance the accuracy of the model.

4. Conclusion

In this study, we developed a dynamic microphysiological system chip platform that can dynamically switch between organ formation mode and blood flow mode for high throughput, customizable microphysiological system construction, and multidimensional drug screening. The intestine, liver, heart, and lung cancer spheroids array were simultaneously cultured by the platform and kept high cell viability for at least five days. A high throughput oral anti-lung cancer drug screening model containing 16 group A549 lung cancer spheroids array was constructed to simultaneously evaluate cisplatin, docetaxel, pemetrexed, and doxorubicin. The evaluation results of four drugs were obtained within one week, and the results demonstrate that doxorubicin was the most effective of the four drugs tested for A549 spheroids. This experiment proves that the MSCP can successfully construct a high throughput drug screening model for more efficient drug screening. We further constructed an intestine(FHs 74 Int)-liver(THLE-2)-heart(HL-1)-lung cancer(A549) microphysiological system to mimic real oral anti-lung cancer drug absorption process, then simultaneously evaluate four oral anti-lung cancer drugs. The results of evaluation showed that the four anti-lung cancer drugs caused varying degrees of damage to the intestine, liver, and heart. Besides, the effectiveness of four oral anti-lung cancer drugs decreased due to the absorption of normal spheroids. This experiment proves that the MSCP can customizable construct microphysiological systems and simultaneously multidimensional evaluate multiple drugs. With these advantages, we believe that the MSCP can be a convenient platform for microphysiological system research, and it has broad application prospects for drug development, re-evaluation, and personalized medicine.

5. Materials and methods

5.1. Fabrication of the MSCP

All the designs of the MSCP were completed by CAD software (AutoCAD 2020, Autodesk Inc.). The MSCP consisted of three PDMS (Polydimethylsiloxane) layers: (1) the microvalve layer containing latitudinal and longitudinal microvalve array. (2) the microchannel layer mainly contains 4 × 4 (row × column) microchannels for different types of spheroid formation, Galton nail plate shaped micropillar arrays, and bubble buffer areas. (3) the microwell layer containing 16 groups of 19-channel honeycomb-shaped microwell arrays. Every microwell has a dimension of 250 × 250 μm (diameter × deep). Three layers are separately made into film masks for further multilayer soft lithography.

After making the film mask, we fabricated the MSCP by photolithography and multilayer soft lithography [67]. A detailed description of the three layers' master mold fabrication can be found in Fig. S5. It is important to note that the master layer of the three-layer structure requires the use of different photoresists to achieve distinct structural characteristics. Specifically, SU8-3025 and SU8-2075 are used for the microvalve layer and microwell layer, respectively, to achieve varying mold thicknesses. To achieve a thin mold thickness and enable the re-flow of the microstructure into a round cross-section for improved microvalve closing effect, AZ40XT-11D is utilized for the microchannel layer.

Once master wafers for each layer were fabricated, we replicated three layers with PDMS (Sylgard 184 silicone elastomer kit, Dow Corning), and then three PDMS replicas were assembled into a functional chip. Detailed descriptions of PDMS replica fabrication and the MSCP assembly can be found in Fig. S6. The punching of holes in the MSCP (multiple-layer PDMS) structure needs to be carried out sequentially. Firstly, holes are punched in the microvalve layer to introduce air pressure. Subsequently, after bonding the microvalve layer to the microchannel layer, holes are punched through both layers. Following this sequence allows for the creation of holes at varying depths.

5.2. Cell culturing

The lung cancer cell line (A549), normal intestinal epithelial cell line (FHs 74 Int), normal liver epithelial cell line (THLE-2), and cardiac muscle cells (HL-1) were used in this research. A549 cells were cultured in RPMI-1640 medium supplemented with 10 % fetal bovine serum (FBS) (Gibco), 1 % penicillin, and streptomycin (Sigma-Aldrich). FHs 74 Int and THLE-2 cells were cultured in Dulbecco's Modified Eagle Medium (DMEM) (Sigma-Aldrich) supplemented with 10 % FBS, 1 % penicillin, and streptomycin. HL-1 cells were cultured in the Calycomb Medium (Sigma-Aldrich) supplemented with 10 % F2442 serum, 1 % Norepinephrine, 1 % L-glutamine, and 1 % penicillin and streptomycin. All four kinds of the cell were cultured at 37 °C in a humidified atmosphere containing 5 % CO_2. Cells would become mature in 3–5 days, and

the medium was changed every 48 h.

5.3. Multiple spheroids formation and evaluation of spheroids viability and histological morphology

Four kinds of spheroids—intestine (FHs 74 Int), liver (THLE-2), heart (HL-1), and lung cancer (A549) were cultivated in the MSCP. Then viability and histological morphology were detected to evaluate these four kinds of spheroids' growth states. Before seeding cells, the MSCP was treated with 1 % pluronic F-127 (Sigma) overnight, sterilized by UV light, and then exchanged the F-127 with PBS (Gibco). Connected all pneumatic microvalves to the pressure controller (ELVEFLOW), and the MSCP was ready to use. For switching the MSCP into organ formation mode, the latitudinal microvalves were closed by applying 500 mbar of air pressure. Then separately resuspended FHs 74 Int, THLE-2, HL-1, and A549 into cell suspension and injected the above-mentioned cell suspension into the MSCP through each cell injection channel. After cells were deposited, redundant cells were washed with PBS. For keeping the nutrients needed for cell growth, the cell culture medium corresponding to each kind of cell was continuously perfusion into the MSCP with 1 μL/min velocity through each cell injection channel. After continuous perfusion culturing, the MSCP was placed into the incubator to keep the temperature, humidity, and gas environment required for spheroids formation. Spheroid growth images were taken by an inverted microscope (NIB900, Nexcope, USA) every 24 h.

5.4. 3D cell viability assay of four different spheroids

After culturing four different cell lines, four different spheroids were generated using Corning® Elplasia® 12K Flask. After expansion for each cell line, the digested suspension containing approximately 10^7 cells was prepared. 30 mL of corresponding culture medium were added to the 12K Flask, followed by the addition of the cell suspension. The 12K Flask was leveled and shaken to evenly distribute cells into each U-bottom well. The 12K Flask was then placed in a humidified, 5 % CO_2, 37 °C incubator for spheroid culture. After two days of culture, the 12K Flask was removed from the incubator, and an appropriate amount of spheroids was extracted from the flask. The extracted spheroids were placed in a 96-well plate with opaque side walls and cultured medium containing the drug was added, with a total volume of 200 μL per well. The plate was then incubated in the incubator for 24 h for drug exposure. Following drug treatment, half of the culture medium was aspirated from each well, and an equal volume of CellTiter-Glo® 3D Cell Viability Assay was added, followed by a 30-min incubation at room temperature. The fluorescence values in each well were quantitatively read using a microplate reader to obtain the raw data. By comparing the viability of spheroids at each drug concentration between the control group without drugs and the experimental group exposed to drug gradients, the IC50 value was calculated.

5.5. High throughput first-line anti-lung cancer drug evaluation by A549 spheroids

Before cell seeding, the MSCP was treated with 1 % pluronic F-127 overnight, sterilized by UV light, washed the MSCP with PBS, and switched the MSCP into organ formation mode. Then A549 cell suspension was injected into the chip through all the cell injection channels. After cells were deposited in the microwell array, redundant cells were flushed by the cell culture medium. The MSCP was placed into the incubator and continuously infused cell culture medium with 1 μL/min. After 72 h culturing, the latitudinal microvalves were opened, and longitudinal microvalves were closed to change the MSCP into the blood flow mode. Four first-line anti-lung cancer drugs—cisplatin, docetaxel, pemetrexed, and doxorubicin were separately prepared into drug-containing cell medium solution with a concentration of 10 μM, 33 μM, 100 μM, 333 μM, and 1000 μM. Then four formula drug-containing medium solutions were simultaneously injected into the MSCP by syringe pump through each drug injection channel and kept injection velocity at 1 μL/min. After 24 h culturing, Calcein-AM/PI (Live/Dead Viability/Cytotoxicity Kit, Dojindo) was added into the cell medium. The mixed solution was injected into the chip and incubated for 30 min at room temperature. The staining solution was washed with PBS. Spheroids' bright field and fluorescence images were acquired using an inverted microscope for cell viability analysis.

5.6. Intestine-liver-heart-lung cancer model establishment and multi-dimensional drug evaluation

The MSCP was prepared according to the above-mentioned process. The device was switched to organ formation mode for different kinds of cell injection. Then FHs 74 Int, THLE-2, HL-1, and A549 cell suspensions were prepared for further seeding. These four kinds of cell suspension were separately injected into the device through the NO.1 to NO.4 cell injection channel. After cells were deposited into the microwell array, redundant cells in each cell injection channel were separately flushed by the corresponding culture medium. The corresponding cell culture medium was continuously injected with a velocity of 1 μL/min. After 72 h culturing, the cells in the microwell array aggregation and formed spheroids then switched the MSCP to blood flow mode. After the flow mode switching, four groups of intestine-liver-heart-lung cancer drug screening models were constructed. The IC_{50} concentration of cisplatin, docetaxel, pemetrexed, and doxorubicin that got from the above single-type spheroid high throughput experiment were applied to prepare each tested drug-containing culture medium (Cisplatin, 109.5 μM; Pemetrexed, 440.1 μM; Doxorubicin, 25.2 μM; Docetaxel, 159.7 μM). Then these four drug-containing culture mediums were simultaneously injected into the MSCP by syringe pump through each drug injection channel and kept injected velocity at 1 μL/min for 24 h. After drug treatment, the Calcein-AM/PI and cell medium mixed solution was injected into the MSCP and incubated for 30 min. PBS was injected into the MSCP to wash the staining solution. An inverted microscope acquired the intestine-liver-heart-lung cancer model's bright-field and fluorescence images to evaluate drug efficacy and side effects further.

5.7. Image data processing

Bright-field and fluorescence sequence images were captured by an inverted microscope (NIB900, Nexcope, USA). The fluorescence sequence images were captured from different z-axis planes. All fluorescence sequence images were stacked on the z-axis. Each microwell's bright-field and fluorescence images were separated from the broad field of view. Then, the fluorescence stack images were converted to RGB stack images. The number of green pixels was read from the live cell fluorescence image. The number of red pixels was read for the dead cell fluorescence image. The number of each spheroid's green and red pixels was recorded, and the total number of green and red pixels was calculated for further statistical analysis.

5.8. Statistical analysis

Each spheroid image was separately segmented from the live/dead staining and bright-field spheroid array images. Cell viability is the proportion of the number of living cell fluorescence pixels to the total number of fluorescence pixels. The IC_{50} value of each first-line anti-lung cancer drug was calculated by the cell viability results of five tested concentrations of each drug. Student's t-tests were used for statistical significance analysis of comprehensive drug evaluation experiments. Drug toxicity results from a standardized difference between one and cell activity. The number of biological duplicates and significance (p) value threshold used for each experiment are listed in figure captions.

Ethics approval and consent to participate

This work does not contain results related to animal or human participant. The cells involved in all the experiments were derived from cell lines.

Data availability

Data will be made available on request.

CRediT authorship contribution statement

Yuxuan Zhu: Writing – review & editing, Writing – original draft, Visualization, Validation, Methodology, Investigation, Formal analysis, Data curation, Conceptualization. **Deming Jiang:** Writing – review & editing, Visualization, Supervision, Methodology, Investigation, Funding acquisition, Conceptualization. **Yong Qiu:** Validation, Methodology, Investigation, Formal analysis. **Xin Liu:** Visualization, Validation, Formal analysis. **Yuhan Bian:** Validation, Methodology, Investigation. **Shichao Tian:** Visualization, Validation, Investigation. **Xiandi Wang:** Supervision, Resources, Methodology, Funding acquisition. **K. Jimmy Hsia:** Supervision, Resources, Project administration, Investigation, Funding acquisition. **Hao Wan:** Writing – review & editing, Supervision, Resources, Project administration, Methodology, Funding acquisition. **Liujing Zhuang:** Writing – review & editing, Validation, Supervision, Resources, Project administration, Methodology, Funding acquisition. **Ping Wang:** Writing – review & editing, Supervision, Resources, Project administration, Funding acquisition.

Declaration of competing interest

The authors declare that they have no known competing financial interests or personal relationships that could have appeared to influence the work reported in this paper.

Acknowledgments

This research was funded by the National Key Research and Development Program of China (No. 2021YFF1200803);National Natural Science Foundation of China (No. 62120106004, 61901412, 62271443); and China Postdoctoral Science Foundation Funded Project (2022M712783).

Appendix A. Supplementary data

Supplementary data to this article can be found online at https://doi.org/10.1016/j.bioactmat.2024.05.019.

References

[1] J. Arrowsmith, P. Miller, Trial watch: phase II and phase III attrition rates 2011-2012, Nat. Rev. Drug Discov. 12 (2013) 569, https://doi.org/10.1038/nrd4090.
[2] R. Ito, T. Takahashi, M. Ito, Humanized mouse models: application to human diseases, J. Cell. Physiol. 233 (2018) 3723, https://doi.org/10.1002/jcp.26045.
[3] I.W. Mak, N. Evaniew, M. Ghert, Lost in translation: animal models and clinical trials in cancer treatment, Am J. Transl. Res. 6 (2014) 114.
[4] B.M. Baker, C.S. Chen, Deconstructing the third dimension: how 3D culture microenvironments alter cellular cues, J. Cell Sci. 125 (2012) 3015, https://doi.org/10.1242/jcs.079509.
[5] Y. Imamura, T. Mukohara, Y. Shimono, et al., Comparison of 2D- and 3D-culture models as drug-testing platforms in breast cancer, Oncol. Rep. 33 (2015) 1837, https://doi.org/10.3892/or.2015.3767.
[6] S.C. Pageau, O.V. Sazonova, J.Y. Wong, et al., The effect of stromal components on the modulation of the phenotype of human bronchial epithelial cells in 3D culture, Biomaterials 32 (2011) 7169, https://doi.org/10.1016/j.biomaterials.2011.06.017.
[7] D. Serra, U. Mayr, A. Boni, et al., Self-organization and symmetry breaking in intestinal organoid development, Nature 569 (2019) 66, https://doi.org/10.1038/s41586-019-1146-y.
[8] S.L. Ryan, A.M. Baird, G. Vaz, et al., Drug discovery approaches utilizing three-dimensional cell culture, Assay Drug Dev. Technol. 14 (2016) 19, https://doi.org/10.1089/adt.2015.670.
[9] J.S. Fleck, F. Sanchis-Calleja, Z. He, et al., Resolving organoid brain region identities by mapping single-cell genomic data to reference atlases, Cell Stem Cell 28 (2021) 1177, https://doi.org/10.1016/j.stem.2021.03.015.
[10] M.A. Lancaster, M. Renner, C.A. Martin, et al., Cerebral organoids model human brain development and microcephaly, Nature 501 (2013) 373, https://doi.org/10.1038/nature12517.
[11] S. Velasco, A.J. Kedaigle, S.K. Simmons, et al., Individual brain organoids reproducibly form cell diversity of the human cerebral cortex, Nature 570 (2019) 523, https://doi.org/10.1038/s41586-019-1289-x.
[12] L. Drakhlis, S. Biswanath, C.M. Farr, et al., Human heart-forming organoids recapitulate early heart and foregut development, Nat. Biotechnol. 39 (2021) 737, https://doi.org/10.1038/s41587-021-00815-9.
[13] P. Hofbauer, S.M. Jahnel, N. Papai, et al., Cardioids reveal self-organizing principles of human cardiogenesis, Cell 184 (2021) 3299, https://doi.org/10.1016/j.cell.2021.04.034.
[14] Y.R. Lewis-Israeli, A.H. Wasserman, M.A. Gabalski, et al., Self-assembling human heart organoids for the modeling of cardiac development and congenital heart disease, Nat. Commun. 12 (2021) 5142, https://doi.org/10.1038/s41467-021-25329-5.
[15] D. Hendriks, B. Artegiani, H.L. Hu, et al., Establishment of human fetal hepatocyte organoids and CRISPR-Cas9-based gene knockin and knockout in organoid cultures from human liver, Nat. Protoc. 16 (2021) 182, https://doi.org/10.1038/s41596-020-00411-2.
[16] Y. Guan, A. Enejder, M. Wang, et al., A human multi-lineage hepatic organoid model for liver fibrosis, Nat. Commun. 12 (2021) 6138, https://doi.org/10.1038/s41467-021-26410-9.
[17] M. Elbadawy, M. Yamanaka, Y. Goto, et al., Efficacy of primary liver organoid culture from different stages of non-alcoholic steatohepatitis (NASH) mouse model, Biomaterials 237 (2020) 119823, https://doi.org/10.1016/j.biomaterials.2020.119823.
[18] L. Broutier, A. Andersson-Rolf, C.J. Hindley, et al., Culture and establishment of self-renewing human and mouse adult liver and pancreas 3D organoids and their genetic manipulation, Nat. Protoc. 11 (2016) 1724, https://doi.org/10.1038/nprot.2016.097.
[19] S.F. Boj, C.I. Hwang, L.A. Baker, et al., Organoid models of human and mouse ductal pancreatic cancer, Cell 160 (2015) 324, https://doi.org/10.1016/j.cell.2014.12.021.
[20] R. Shi, N. Radulovich, C. Ng, et al., Organoid cultures as preclinical models of non-small cell lung cancer, Clin. Cancer Res. 26 (2020) 1162, https://doi.org/10.1158/1078-0432.CCR-19-1376.
[21] M. Kim, H. Mun, C.O. Sung, et al., Patient-derived lung cancer organoids as in vitro cancer models for therapeutic screening, Nat. Commun. 10 (2019) 3991, https://doi.org/10.1038/s41467-019-11867-6.
[22] E. Yokota, M. Iwai, T. Yukawa, et al., Clinical application of a lung cancer organoid (tumoroid) culture system, npj Precis. Oncol. 5 (2021) 29, https://doi.org/10.1038/s41698-021-00166-3.
[23] A. Grapin-Botton, Three-dimensional pancreas organogenesis models, Diabetes Obes. Metabol. 18 (Suppl 1) (2016) 33, https://doi.org/10.1111/dom.12720.
[24] M.A. Lancaster, J.A. Knoblich, Organogenesis in a dish: modeling development and disease using organoid technologies, Science 345 (2014) 1247125, https://doi.org/10.1126/science.1247125.
[25] R. Ramezankhani, R. Solhi, Y.C. Chai, et al., Organoid and microfluidics-based platforms for drug screening in COVID-19, Drug Discov. Today 27 (2022) 1062, https://doi.org/10.1016/j.drudis.2021.12.014.
[26] K. Achberger, M. Cipriano, M.J. Duchs, et al., Human stem cell-based retina on chip as new translational model for validation of AAV retinal gene therapy vectors, Stem Cell Rep. 16 (2021) 2242, https://doi.org/10.1016/j.stemcr.2021.08.008.
[27] Y. Zhu, L. Wang, H. Yu, et al., In situ generation of human brain organoids on a micropillar array, Lab Chip 17 (2017) 2941, https://doi.org/10.1039/c7lc00682a.
[28] Y.Q. Wang, L. Wang, Y.J. Zhu, et al., Human brain organoid-on-a-chip to model prenatal nicotine exposure, Lab Chip 18 (2018) 851, https://doi.org/10.1039/c7lc01084b.
[29] A.N. Cho, Y. Jin, Y. An, et al., Microfluidic device with brain extracellular matrix promotes structural and functional maturation of human brain organoids, Nat. Commun. 12 (2021) 4730, https://doi.org/10.1038/s41467-021-24775-5.
[30] Y.S. Zhang, A. Arneri, S. Bersini, et al., Bioprinting 3D microfibrous scaffolds for engineering endothelialized myocardium and heart-on-a-chip, Biomaterials 110 (2016) 45, https://doi.org/10.1016/j.biomaterials.2016.09.003.
[31] M. Abulaiti, Y. Yalikun, K. Murata, et al., Establishment of a heart-on-a-chip microdevice based on human iPS cells for the evaluation of human heart tissue function, Sci. Rep. 10 (2020) 19201, https://doi.org/10.1038/s41598-020-76062-w.
[32] S. Ya, W. Ding, S. Li, et al., On-chip construction of liver lobules with self-assembled perfusable hepatic sinusoid networks, ACS Appl. Mater. Interfaces 13 (2021) 32640, https://doi.org/10.1021/acsami.1c00794.
[33] J. Lee, B. Choi, Y. No da, et al., A 3D alcoholic liver disease model on a chip, Integr. Biol. 8 (2016) 302, https://doi.org/10.1039/c5ib00298b.
[34] Y. Hu, X. Sui, F. Song, et al., Lung cancer rganoids analyzed on microwell arrays predict drug responses of patients within a weeko, Nat. Commun. 12 (2021) 2581, https://doi.org/10.1038/s41467-021-22676-1.
[35] Y. Wang, H. Wang, P. Deng, et al., In situ differentiation and generation of functional liver organoids from human iPSCs in a 3D perfusable chip system, Lab Chip 18 (2018) 3606, https://doi.org/10.1039/c8lc00869h.

[36] T.T. Tao, P.W. Deng, Y.Q. Wang, et al., Microengineered multi-organoid system from hiPSCs to recapitulate human liver-islet Axis in normal and type 2 diabetes, Adv. Sci. 9 (2022), https://doi.org/10.1002/advs.202103495. ARTN 2103495.
[37] F. Yin, X. Zhang, L. Wang, et al., HiPSC-derived multi-organoids-on-chip system for safety assessment of antidepressant drugs, Lab Chip 21 (2021) 571, https://doi.org/10.1039/d0lc00921k.
[38] K. Ronaldson-Bouchard, D. Teles, K. Yeager, et al., A multi-organ chip with matured tissue niches linked by vascular flow, Nat. Biomed. Eng. 6 (2022) 351, https://doi.org/10.1038/s41551-022-00882-6.
[39] S. Abizanda-Campo, M. Virumbrales-Munoz, M. Humayun, et al., Microphysiological systems for solid tumor immunotherapy: opportunities and challenges, Microsyst Nanoeng 9 (2023) 154, https://doi.org/10.1038/s41378-023-00616-x.
[40] J.M. Ayuso, M. Farooqui, M. Virumbrales-Muñoz, et al., Microphysiological model reveals the promise of memory-like natural killer cell immunotherapy for HIV± cancer, Nat. Commun. 14 (2023), https://doi.org/10.1038/s41467-023-41625-8.
[41] M. Trapecar, Multiorgan microphysiological systems as tools to interrogate interorgan crosstalk and complex diseases, FEBS Lett. 596 (2022) 681, https://doi.org/10.1002/1873-3468.14260.
[42] Y.I. Wang, C. Carmona, J.J. Hickman, et al., Multiorgan microphysiological systems for drug development: strategies, advances, and challenges, Adv. Healthcare Mater. 7 (2018), https://doi.org/10.1002/adhm.201701000.
[43] T. Ahmed, Organ-on-a-chip microengineering for bio-mimicking disease models and revolutionizing drug discovery, Biosens. Bioelectron. X 11 (2022), https://doi.org/10.1016/j.biosx.2022.100194.
[44] H.N. Kim, N.L. Habbit, C.Y. Su, et al., Microphysiological systems as enabling tools for modeling complexity in the tumor microenvironment and accelerating cancer drug development, Adv. Funct. Mater. 29 (2019), https://doi.org/10.1002/adfm.201807553.
[45] J. Ko, J. Song, N. Choi, et al., Patient-derived microphysiological systems for precision medicine, Adv. Healthcare Mater. (2023), https://doi.org/10.1002/adhm.202303161e2303161, 10.1002/adhm.202303161.
[46] I. Maschmeyer, T. Hasenberg, A. Jaenicke, et al., Chip-based human liver-intestine and liver-skin co-cultures–A first step toward systemic repeated dose substance testing in vitro, Eur. J. Pharm. Biopharm. 95 (2015) 77, https://doi.org/10.1016/j.ejpb.2015.03.002.
[47] I. Maschmeyer, A.K. Lorenz, K. Schimek, et al., A four-organ-chip for interconnected long-term co-culture of human intestine, liver, skin and kidney equivalents, Lab Chip 15 (2015) 2688, https://doi.org/10.1039/c5lc00392j.
[48] M. Trapecar, E. Wogram, D. Svoboda, et al., Human physiomimetic model integrating microphysiological systems of the gut, liver, and brain for studies of neurodegenerative diseases, Sci. Adv. 7 (2021), https://doi.org/10.1126/sciadv.abd1707. ARTN eabd1707.
[49] H.B. Choi, J.S. Pyo, S. Son, et al., Diagnostic and prognostic roles of CDX2 immunohistochemical expression in colorectal cancers, Diagnostics 12 (2022), https://doi.org/10.3390/diagnostics12030757.
[50] S. Khurana (Ed.), Aspects of the Cytoskeleton, 2006, p. 89, https://doi.org/10.1016/s1569-2558(06)37005-1.
[51] A.K. Daly, A.E. Rettie, D.M. Fowler, et al., Pharmacogenomics of CYP2C9: functional and clinical considerations, J. Personalized Med. 8 (2017), https://doi.org/10.3390/jpm8010001.
[52] R.J. Schulze, M.B. Schott, C.A. Casey, et al., The cell biology of the hepatocyte: a membrane trafficking machine, J. Cell Biol. 218 (2019) 2096, https://doi.org/10.1083/jcb.201903090.
[53] K.G. Oikonomou, K. Zachou, G.N. Dalekos, Alpha-actinin: a multidisciplinary protein with important role in B-cell driven autoimmunity, Autoimmun. Rev. 10 (2011) 389, https://doi.org/10.1016/j.autrev.2010.12.009.
[54] R.Y. Xu, X.F. Zhu, Y. Yang, et al., High-sensitive cardiac troponin T, J. Geriatr Cardiol. 10 (2013) 102, https://doi.org/10.3969/j.issn.1671-5411.2013.01.015.
[55] H.T. Luo, C.X. Liang, R.C. Luo, et al., Identification of relevant prognostic values of cytokeratin 20 and cytokeratin 7 expressions in lung cancer, Biosci. Rep. 37 (2017), https://doi.org/10.1042/BSR20171086.
[56] A.M. Mendonsa, T.Y. Na, B.M. Gumbiner, E-cadherin in contact inhibition and cancer, Oncogene 37 (2018) 4769, https://doi.org/10.1038/s41388-018-0304-2.
[57] C.E. Oturanel, I. Kiran, O. Ozsen, et al., Cytotoxic, antiproliferative and apoptotic effects of perillyl alcohol and its biotransformation metabolite on A549 and HepG2 cancer cell lines, Anti Cancer Agents Med. Chem. 17 (2017) 1243, https://doi.org/10.2174/1871520617666170103093923.
[58] C.C. Tieche, Y. Gao, E.D. Buhrer, et al., Tumor initiation capacity and therapy resistance are differential features of EMT-related subpopulations in the NSCLC cell line A549, Neoplasia 21 (2019) 185, https://doi.org/10.1016/j.neo.2018.09.008.
[59] M.I. Khot, M.A. Levenstein, G.N. de Boer, et al., Characterising a PDMS based 3D cell culturing microfluidic platform for screening chemotherapeutic drug cytotoxic activity, Sci. Rep. 10 (2020) 15915, https://doi.org/10.1038/s41598-020-72952-1.
[60] B. Schuster, M. Junkin, S.S. Kashaf, et al., Automated microfluidic platform for dynamic and combinatorial drug screening of tumor organoids, Nat. Commun. 11 (2020), https://doi.org/10.1038/s41467-020-19058-4. ARTN 5271.
[61] N. Dadgar, A.M. Gonzalez-Suarez, P. Fattahi, et al., A microfluidic platform for cultivating ovarian cancer spheroids and testing their responses to chemotherapies, Microsy. Nanoeng 6 (2020), https://doi.org/10.1038/s41378-020-00201-6.
[62] Y. Peng, E. Lee, Microphysiological systems for cancer immunotherapy research and development, Adv. Biol. (Weinh) (2023), https://doi.org/10.1002/adbi.202300077e2300077, 10.1002/adbi.202300077.
[63] A. Skardal, J. Aleman, S. Forsythe, et al., Drug compound screening in single and integrated multi-organoid body-on-a-chip systems, Biofabrication 12 (2020) 025017, https://doi.org/10.1088/1758-5090/ab6d36.
[64] P.S. Rawat, A. Jaiswal, A. Khurana, et al., Doxorubicin-induced cardiotoxicity: an update on the molecular mechanism and novel therapeutic strategies for effective management, Biomed. Pharmacother. 139 (2021) 111708, https://doi.org/10.1016/j.biopha.2021.111708.
[65] C.F. Thorn, C. Oshiro, S. Marsh, et al., Doxorubicin pathways: pharmacodynamics and adverse effects, Pharmacogenetics Genom. 21 (2011) 440, https://doi.org/10.1097/FPC.0b013e32833ffb56.
[66] H.A. Burris, Optimal use of docetaxel (Taxotere): maximizing its potential, Anti Cancer Drugs 7 (Suppl 2) (1996) 25.
[67] K. Brower, A.K. White, P.M. Fordyce, Multi-step variable height photolithography for valved multilayer microfluidic devices, J. Vis. Exp. (2017), https://doi.org/10.3791/55276, 10.3791/55276.